Original Paper

Pore Fabric Anisotropy of the Cambrian–Ordovician Nubia Sandstone in the Onshore Gulf of Suez, Egypt: A Surface Outcrop Analog

Nader T. H. Elgendy,[1] Bassam A. Abuamarah,[2,5] Bassem S. Nabawy,[3] Habes Ghrefat,[2] and Osama M. K. Kassem[2,4]

Integrated studies on pore fabric anisotropy have increased the general understanding of fluid flow patterns through reservoir rocks. In this study, pore anisotropy was studied based on measuring permeability and formation resistivity factors in vertical and horizontal directions for 130 plug samples from a total of 65 oriented block samples. These samples were representatively collected for the Nubia sandstones C and D in the western southern onshore of the Gulf of Suez. In addition, the porosity was measured using two techniques, namely water and helium injection. The effective pore radius r_{35} and the pore radius of the displacement pressure (r_{dp}) were also measured. Petrographic studies of some representative thin sections and scanning electron microscope studies (SEM) were applied to study the mineral compositions of the studied samples to declare the most important porosity-reducing and porosity-enhancing diagenetic factors. The results show that the studied samples can be categorized into three rock types (RRTs), namely quartz arenite (RRT1), quartz wacke (RRT2) and mudstone (RRT3). The best storage and flow capacity was assigned to the RRT1 samples, whereas the least quality was assigned to the RRT3 samples. This could be attributed to wide pore throat distributions and the anisotropy of pore spaces due to the presence of a vertical subsidiary fracture system that dominated in many samples. This system was enhanced by introducing authigenic kaolinite as pore-filling clay minerals, causing the reduction in vertical permeability but supporting the vertical electric current flow. For the RRT3 samples, this vertical micro-fracture system was reduced by silica cementation which caused the reduction in both fluid and electric current flow. The pore anisotropy of most of the studied samples is in the range of slight anisotropy with some exceptions in the RRT3 samples which are characterized by moderate anisotropy.

KEY WORDS: Nubia sandstone, Electric pore anisotropy, Foliation, Lineation, Permeability, Porosity.

[1]Geology Department, Faculty of Science, Tanta University, Tanta, Egypt.

[2]Department of Geology & Geophysics, College of Science, King Saud University, Riyadh, Kingdom of Saudi Arabia.

[3]Department of Geophysical Sciences, National Research Center, Dokki, Cairo, Egypt.

[4]Department of Geological Sciences, National Research Center, Dokki, Cairo, Egypt.

[5]To whom correspondence should be addressed; e-mail: babuamarah@ksu.edu.sa

INTRODUCTION

The term Nubia sandstone is well established in the lithostratigraphic column of Egypt. It refers to a thick sequence of pre-Cenomanian sandy formations overlying the Precambrian basement rocks and conformably underlying the Cenomanian marine sequences (Fig. 1). This sequence of sandy forma-
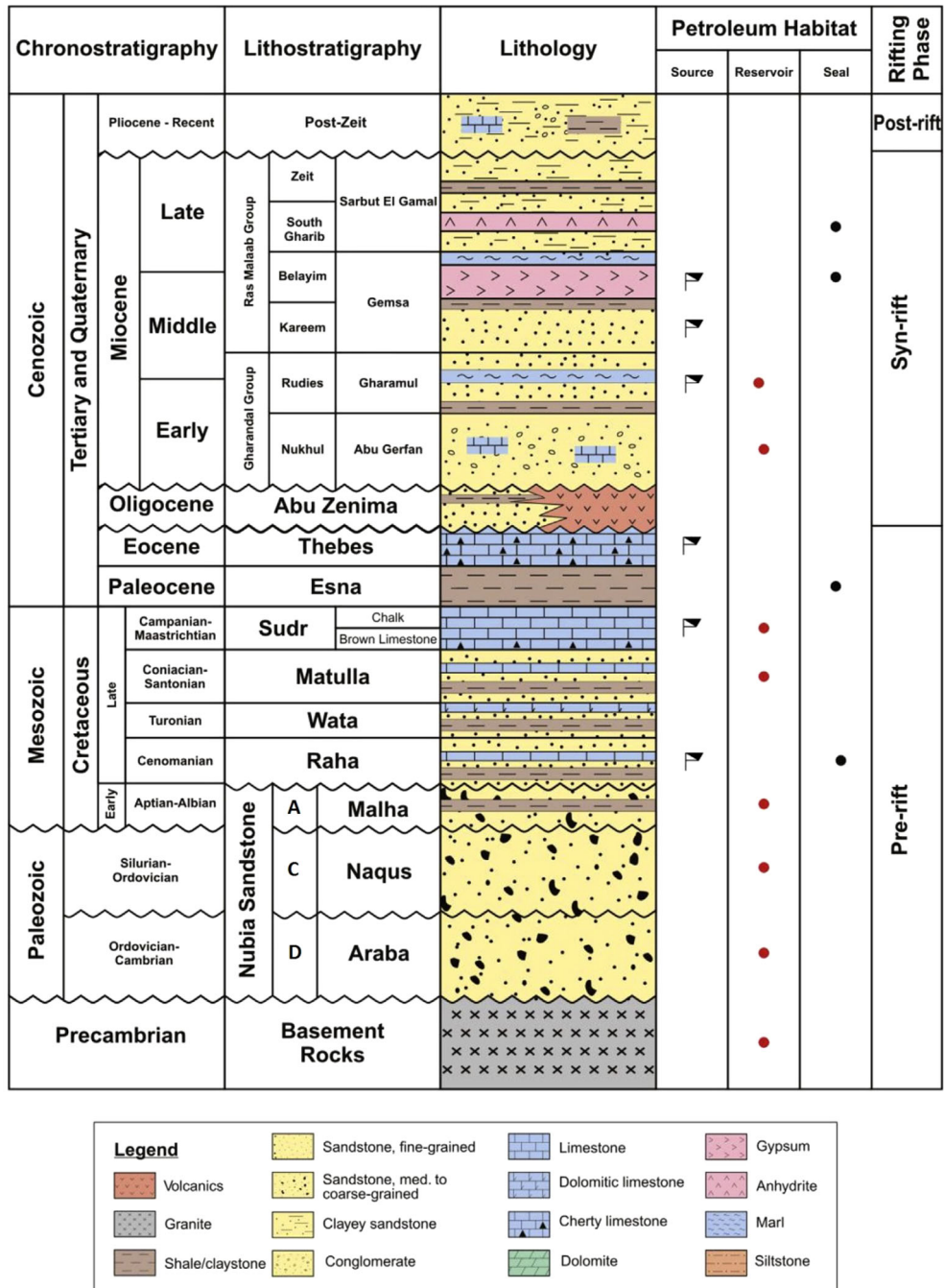
Fig. 1. Generalized stratigraphic section of the southern Gulf of Suez. Modified after Schlumberger (1984, 1995), EGPC (1996) and Sakran et al. (2016).

tions covers vast areas of Egypt with a broad age window ranging from the Cambrian to Aptian–Albian geological timescales. The Paleozoic Nubia sandstone in the northern parts of the Eastern Desert is composed of nonfossiliferous, fine- to coarse-grained and well-rounded sandstone. It sometimes contains gravel and pebbles, and it is cross-bedded at different horizons. It comprises 355 m of fine- to coarse-grained quartz arenite with few thin pebbly beds. In the southwest onshore Gulf of Suez, the

A Surface Outcrop Analog

Nubia sandstone is divided into the well-known Araba and Naqus Formations (Allam 1988; Abdel-Wahab 1988, 1998). The Araba Formation unconformably overlies the Precambrian basement and is of marine origin with a thickness varying from 1 to 35 m. Its maximum thickness lies at the center of the section (Hassan 1967; Said 1971). The Naqus Formation unconformably overlies the Araba Formation and a rough undulated surface with a paleosol layer in certain places (Issawi and Jux 1982; Issawi et al. 1999). It is composed of about 320 m of well-sorted, laminated, fine- to medium-grained, reddish-brown and cross-bedded fluvial sandstone. The Araba and Naqus Formations unconformably rest on the basement rocks bounding the Gulf of Suez and do not have diagnostic fossils that are necessary for a distinct age determination. Therefore, their age has been assigned based on the stratigraphic sequences in the area. In general, the Nubia sandstone is nonfossiliferous, fine to coarse-grained, sometimes pebbly, well-rounded, cross-bedded sandstone with some ferruginous and shaly interbeds.

The Nubia sandstone in the study area has been studied by many authors who have examined the sedimentological properties, structural situation and the paleo-depositional environments. The pore fabric anisotropy in the Nubia sandstone has been studied by many authors based on the petrographic descriptions of the pore shape and pore aspect (Ehrlich et al. 1984; Etris et al. 1988; Antonellini et al. 1994; Torabi and Fossen 2009; Schmitt et al. 2016; Farrell and Healy 2017), the anisotropy of permeability (Etris et al. 1988; David et al. 1994; Lucia 1995; Caine et al. 1996; Meyer and Krause 2006; Khan et al. 2012; Farrell et al. 2014), the anisotropy induced by compaction stresses and acoustic waves (David et al. 1994; Benson et al. 2003; Takemura et al. 2003; Healy 2012; Bubeck et al. 2017), the anisotropy of magnetic susceptibility, AMS (Jelinek 1981; Rochette 1987; Benson et al. 2003; Borradaile and Jackson 2004; Levi et al. 2005; Jayangondaperumal et al. 2010), thermal conductivity (Nabawy and Géraud 2016) and electric anisotropy measurements (Mendelson and Cohen 1982; Nabawy and ElHariri 2008; Ellis et al. 2010; Guo et al. 2011; Soto-Cabán and Law 2013; Nabawy et al. 2015).

The present study is concerned mostly with the pore fabric anisotropy of the Nubia sandstone sequences in the northern parts of the Eastern Desert in Egypt by using permeability and electric resistivity measurements to reveal the factors that control these features. This is an important preliminary petrophysical study that focuses on the pore fabric of the Paleozoic Nubia sandstone. This sandstone has a subsurface extension in the southern province of the Gulf of Suez and many surface outcrops in the southern parts of Sinai in Egypt.

MATERIALS AND METHODS

A total of 130 plugs were drilled through the selected 65 oriented surface block samples (two plugs per block, in vertical and horizontal directions relative to the sedimentary bedding) that were representatively selected for the Nubia sandstone in the study area. Ten blocks were in the Araba Formation, and 55 blocks were in the Naqus Formation. The mineral composition was studied using a number of thin sections impregnated by a blue dye and stained with Alizarin Red-S. Some representative rock fragments were also studied using scanning electron microscopy (SEM) to investigate the pore anisotropy and clay types.

The plug samples were then cleaned and dried in an oven at 60°C for 48 h. The bulk density (ρ_b) was quantified based on the bulk volume (v_b) and dry weight (w_{dry}) of the samples. The bulk volume and dimensions of the studied samples were measured using a digital micrometer (with 0.01 mm precision), whereas the dry weight was measured using an electronic balance (with 0.1 mg precision):

$$\rho_b = w_{dry}/v_b. \qquad (1)$$

In addition, the porosity of the studied samples was measured by the injection technique using two fluids, namely water and helium (ϕ_w, ϕ_{He}, respectively). The helium injection porosity was determined by measuring the grain (v_g) and bulk volumes (v_b) of the studied samples using a helium pycnometer (whereby helium was injected at 19 psi). Therefore, based on the bulk and grain volumes (v_b, v_g), the helium porosity (ϕ_{He}) and the grain density (ρ_g), in addition, were calculated by following the procedure introduced by Nabway and Kassab (2014):

$$\phi_{He} = 100 \times (v_b - v_g)/v_b \qquad (2)$$

$$\rho_g = w_{dry}/v_g \qquad (3)$$

The water porosity (ϕ_w) was measured using water injection whereby the samples were weighted

dry (w_{dry}) and evacuated using evacuation pump (down to 0.001 bar) for 2 h, and then fully saturated with distilled water. The samples were weighed again after saturation (w_{sat}) took place, and the following equation was applied:

$$\phi_w\,(\%) = 100 \times (v_p/v_b) = 100 \times (w_{sat} - w_{dry})/v_b \tag{4}$$

where v_p is the pore volume assuming that the density of the injected water equals unity.

Helium porosity is always higher than water porosity, because helium can penetrate pores down to 10 nm, whereas water is unable penetrate nanopores due to its relatively larger molecular size. Therefore, the difference between helium and water porosities may refer to nano- and micropores which are not accessible to water injection. Inaccessible porosity (ϕ_{inacc}) can be calculated by using the following equation (Nabawy et al. 2019):

$$\phi_{inacc} = 100 \times (1 - \phi_W/\phi_{He}) \tag{5}$$

Permeability (k) was measured using an air gas permeameter whereby the samples are introduced into a Hassler-type core holder to prevent bypass using a pressure of 27.58 bar (400 psi). To measure the pore anisotropy, the permeability was measured for the vertical and horizontal plug samples (k_H and k_V) in each block sample. Porosity varies slightly from place to place in the same lithofacies, a slight variation can be detected in even the same block sample. Therefore, the contribution of porosity to permeability varies from the horizontal plug to the vertical plug (Nabawy 2018). For the present study, the permeability value of the vertical plug (the porosity of this plug is slightly different from that of the horizontal plug) was corrected (k_{VC}) for the same porosity value of the horizontal plug sample in order to avoid variations in the porosity contribution. The correction was applied using the best-fit line model for the porosity–vertical permeability by using the porosity of the horizontal plug. The permeability anisotropy can be calculated by using the following equation (Nabawy 2018):

$$\lambda_{kC} = \sqrt{(k_H/k_{VC})} \tag{6}$$

A full description of the applied method was introduced by Nabawy (2014), and Nabway and Kassab (2014). The apparent electrical conductivity (σ_r) measurements were carried out at a fixed frequency (1 kHz) on saline-saturated plug samples using an LCR Hitester meter (a device that assigns inductance L, capacitance C and resistance R) at three consequent saline concentrations, 10, 50 and 150 kppm NaCl (σw = 1.887, 7.692 and 20 Siemens/m, respectively). The measurements were carried out under surface ambient conditions at atmospheric pressure and room temperature. The true formation resistivity factor (FR_T) for each sample was then calculated by plotting the measured rock conductivity (σ_r) at different brine concentrations vs. its brine conductivity (σ_w). The FR_T was obtained as the reciprocal of the best-fit line slope ($1/FR_T$). A detailed description of the applied method was introduced by Nabawy and ElHariri (2008), and Nabawy et al. (2015). To interpret the electric anisotropy, two plugs (from each block) were measured parallel and perpendicular to the bedding plane. Measuring the two perpendicular plug samples enabled an estimation of the electric anisotropy in 2-D (λ_E) for each block sample (Serra 1988; Nabawy and ElHariri 2008; Nabawy et al. 2015).

Similar to calculating the permeability anisotropy, the calculated electric anisotropy was measured for two perpendicular samples (each with a different porosity value). Therefore, the corrected electric anisotropy (λ_{EC}) was then corrected for the same porosity values and the anisotropy could be calculated as follows:

$$\lambda_{EC} = \sqrt{(FR_{VC}/FR_H)} \quad (\text{Nabawy 2018}) \tag{7}$$

where FR_H is the formation resistivity factor in the horizontal direction and FR_{VC} is FR_V in the vertical direction corrected for the same porosity value of the horizontal direction.

The pore throat distribution was estimated using the mercury injection capillary pressure technique (MICP) at a pressure range of up to 30,000 psi for a representative number of samples whereby the higher the applied pressure, the smaller the assigned pore throat radius (Nabawy and Barakat 2017). From this plot, the r_{35} pore radius of Winland (1972), as well as the r_{dp} (Schowalter 1979), was calculated. The r_{35} is defined as the pore throat size corresponding to the 35th percentile of the cumulative mercury saturation curve as a function of the applied pressure. The r_{dp} is the pore throat size corresponding to the tenth percentile of the cumulative mercury saturation curve. This pore size corresponds to the pressure needed for starting the fluid displacement inside the pore spaces. It is important to note that these measurements were carried out in a laboratory at surface ambient conditions and on a

surface analog. The properties at various depths are probably different due to the impacts of burial as well as lateral facies changes. Therefore, corrections must be applied by taking geo-pressures into consideration.

THE STUDY AREA

Geological and Structural Setting

Although the western coast of the Gulf of Suez has been studied by many authors, only a few studies have been published on the petrophysics, mineralogy and diagenetic history of the Cambrian–Ordovician Nubia sandstone sequence in the studied area. In addition, no detailed studies have been introduced on the pore fabric and petrophysical anisotropy of the Nubia sandstone along the Gulf of Suez shore lines.

Most of the previous studies concentrated on structure and general geology, while other studies investigated the stratigraphy of the Gulf of Suez (El-Gindi 1972; Zein El-Din and Taher 1973; Perry 1977; Perry and Schamel 1982; Angelier 1985; Youssef 1986; Colletta et al. 1986; Abdel-Wahab 1988, 1998; Allam 1988, 1989; Abdallah et al. 1992a, b; Schütz 1994; Ibrahim 1996; Salem et al. 1998; Issawi et al. 1999; Aboud et al. 2005; Nabawy and El Sharawy 2015; El Sharawy and Nabawy 2016a, b; Nabawy and Barakat 2017). In southwest Gulf of Suez, the Nubia sandstone is classified into Nubia D (35.0 m) and C (320.0 m), which are collectively referred to by many authors as the Araba and Naqus Formations (Schlumberger 1984, 1995).

Tectonically, the Gulf of Suez represents a great elongated depression of 400 km in length separating the Sinai Peninsula from the Egyptian mainland. In fact, the Gulf of Suez region represents one of the most intensively faulted areas of Egypt. Its structure is mostly dominated by normal faults and tilted blocks trending in NW–SE, with sedimentary fill up to 6 km thick (Jackson et al. 1988).

The study area, at Gebel El-Zeit area in particular, is characterized by a basin structural system trending NW–SE parallel to the Red Sea main trend. It represents the complex arched structural style of Gebel El-Zeit that is reflected by complex arches in the major downthrown block to the east and in a minor buried horst block to the west. It is a typical example of the complex structures of the Gulf of Suez region. It is characterized by two main faults,

namely the Zeit fault to the east that trends NE–SW and the Ras El-Dib fault to the west that trends NW–SE, parallel to the Gulf of Suez (Fig. 2). These two faults form a graben system structure that takes the direction of NW–SE. These faults brought the granite mass of the northern part of the Esh El-Mellaha and Gebel El-Zeit ranges into juxtaposition with the Paleozoic sedimentary sequences. In addition, several minor intersected faults and fractures are recognized at the western and eastern parts of Gebel El-Zeit. Zeit and Mellaha are the major basement blocks in Gebel El-Zeit, dipping 5° to 35° tilted to the SW and bounded by large normal faults to the NE. The titled blocks generally trend N145–150°E, parallel to the axis of the Gulf of Suez. The deposition of the sedimentary sequences occurred around the basement core of the Gebel El-Zeit range (Farouk 1965; Perry 1977; Angelier 1985; Allam 1988). Gebel El-Zeit is a well-known natural oil seepage field in the southern province of the Gulf of Suez with its main pay zone located through the eroded crest of a tilted block displaying a typical asymmetrical structure. This crest remained as a high stand position during most of the Cenozoic history, but its overall evolution was similar to that of the Gulf of Suez rift (Colletta et al. 1986).

In general, the Gebel El-Zeit area can be subdivided into four separate structural provinces (Fig. 2); (1) the main Zeit range, (2) the Ras El-Ush graben, (3) the South Zeit range and (4) the West Zeit range (Hagras 1986). The faults in the Gebel El-Zeit area follow several trends with the majority of them trending parallel to the Gulf of Suez (Allam 1988; Sakran et al. 2016; Fig. 3).

Lithostratigraphy

The Nubia sandstone in southwest Gulf of Suez is composed of Cambrian Nubia D (Araba Formation) and the Ordovician Nubia C (Naqus Formation) (Hassan 1967; Allam 1988; Abdel-Wahab 1988, 1998; David et al. 2015; Nabawy and David 2016; Nabawy et al. 2018, 2019). Nubia D (35 m) is barren of fossils and consists of cross-bedded medium- to coarse-grained sandstones. It rests unconformably on the underlying weathered granite with an undulatory kaolinitic thin zone where some pebbles and gravel follow upward alongside 10 m of dark red and medium-grained sandstones (Fig. 1). The middle parts are composed of 5.0 m of shaly sand (Fig. 4a) and 3.0 m of gravelly to pebbly dark brown sand-
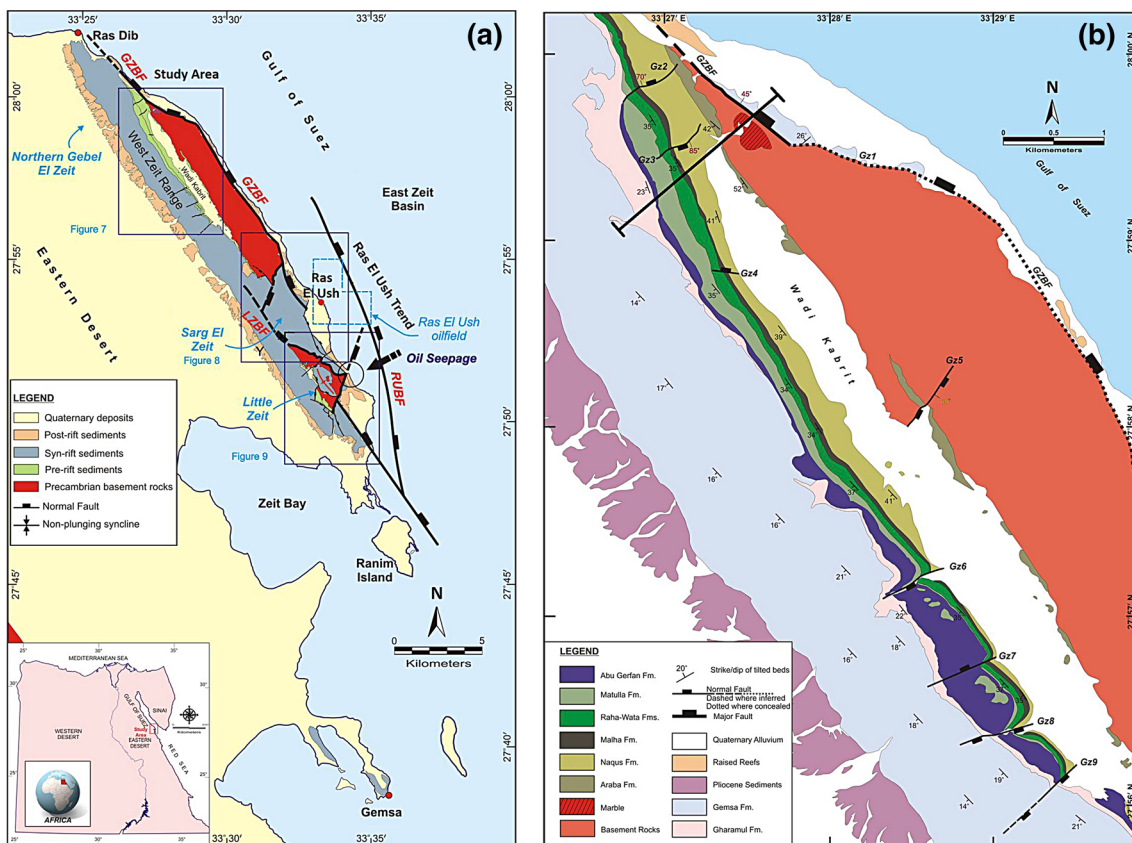
Fig. 2. Compiled geological and structural map of (**a**) Gebel El-Zeit area and (**b**) the study area in Gebel El-Zeit, Gulf of Suez, Egypt (Sakran et al. 2016).
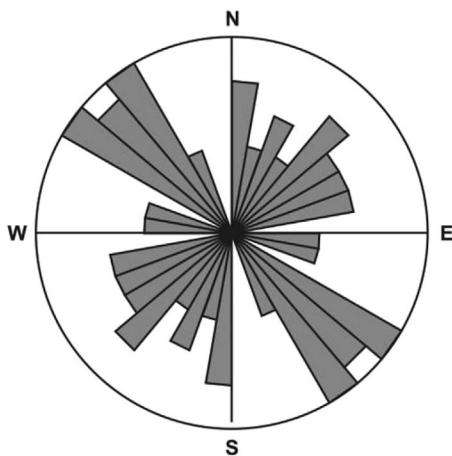
Fig. 3. Strike summary plot showing fault frequency distribution in the Gebel El-Zeit area (Allam 1988; Sakran et al. 2016).

stone. Above this level, there are two main beds of medium- to coarse-grained reddish sandstones (7.0 m) and fine- to coarse-grained reddish-to-violet cross-bedded sandstone (10 m).

Upward, the sandstone of the Ordovician Nubia C (320 m) is overlain unconformably by the carboniferous and the Cretaceous deposits (e.g., Abdallah and Adindani 1963; Said 1971; Kora 1984; Klitzsch 1986; Beleity et al. 1986; Allam 1988; Khalifa et al. 2006; Nabawy et al. 2018). It consists mostly of well-sorted, cross-bedded fine- to medium-grained white quartz arenite with some shale intercalations (Fig. 2). The presence of some poorly sorted pebbles and gravel that are randomly distributed within the Nubia C is one of its most diagnostic features (Wanas 2011; Nabawy et al. 2019).

The lower parts of the Nubia C are composed of 90.0 m of white-to-varicolored coarse- to medium-grained and cross-bedded sandstones, coarsening upward with some gravel. Upward, the middle parts
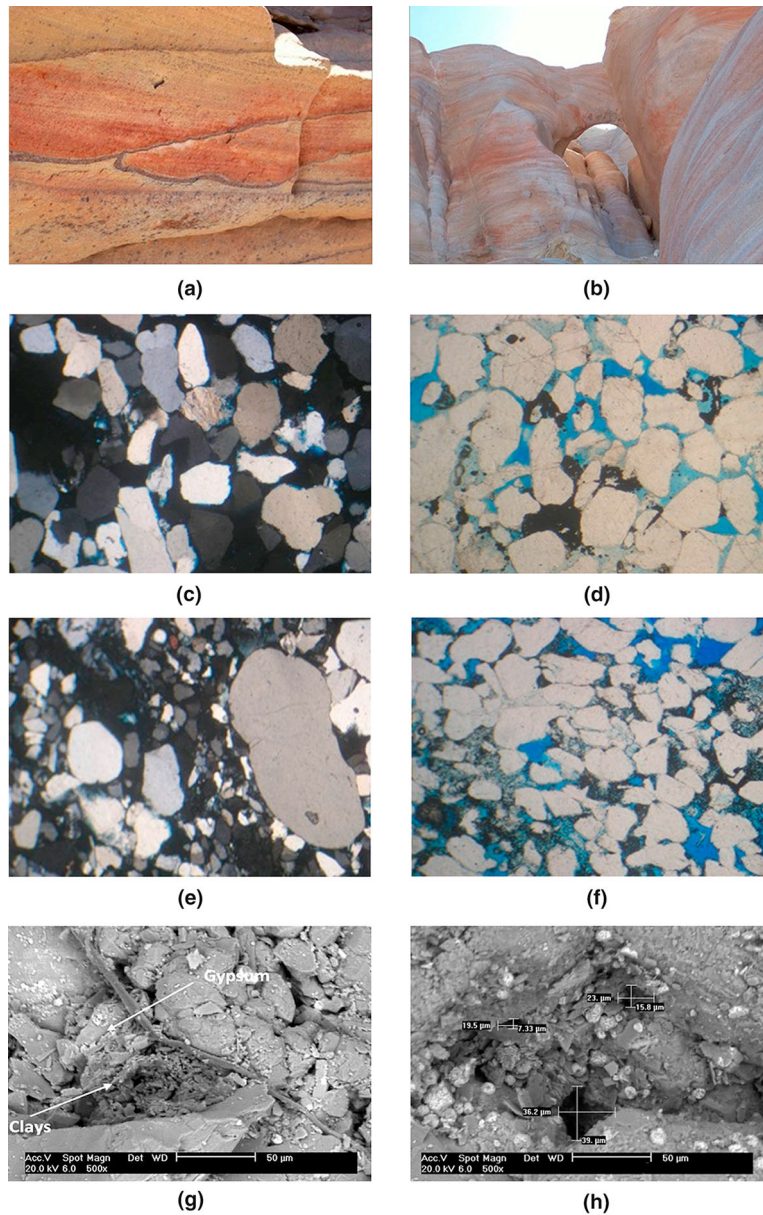
Fig. 4. Field photographs of: (**a**) reddish-brown laminated shaly sandstone representing the lower part of Nubia C sequence and (**b**) reddish to yellowish-white cross-laminated sandstones of the topmost parts of Nubia C. The photomicrographs show: (**c**) poorly sorted, very fine- to coarse-grained, angular to subrounded quartz grains that have wavy extinction and are rarely polycrystalline, highly compacted and long to suture grain contact with some gypsum content. These rocks comprise quartz arenite micro-facies in the topmost parts of Nubia D, C.N., 40X; (**d**) moderately sorted cloudy quartz grains, fine to coarse grained, subangular to rounded and slightly compacted in point contacts. These pore spaces are mostly intergranular, and some quartz grains have micro-fractures. Sometimes, the pore spaces are reduced by filling clay patches. These samples comprise quartz arenite micro-facies in the basal parts of Nubia C, PPL, 40X. (**e**) Ill-sorted quartz grains, very fine to very coarse grained, angular to rounded, highly compacted together with some orientation. Corrosion is noticed at the borders of some grains. These rocks comprise quartz arenite micro-facies in the middle parts of Nubia C, C.N, 40X. (**f**) Moderately sorted, very fine quartz grains, compacted together with good to very good intergranular porosity, partially filled by gypsum and clay patches. These rocks comprise the quartz wacke micro-facies of the Nubia C, PPL, 40X. The SEM photomicrographs show: (**g**) intergranular and fracture porosity reduced by clay content and gypsum laminae. These rocks comprise quartz arenite micro-facies in the middle to top parts of Nubia D, and (**h**) macro- (pore size ≥ 75 μm) to meso- (75 μm ≥ pore size ≥ 30 μm) intergranular pore spaces partially reduced by gypsum and clay content. These rocks comprise the quartz wacke micro-facies in the middle to top parts of Nubia C

consist of 107 m of medium- to coarse-grained, cross-bedded, friable and tight sandstones with slight pebbly content.

The topmost parts of the Nubia C are composed of varicolored, medium- to coarse-grained, jointed, cross-laminated friable sand and sandstones topped with friable conglomeratic sandstones (Fig. 4b) (Nabawy et al. 2018, 2019).

RESULTS

Mineral Composition

Petrographically, both Nubia C and D are similar in composition to one another. Therefore, for the present study, it is recommended that the sequence should be dealt with as one bulk sequence. The studied Nubia sequence is composed of three micro-facies and rock types (RRTs): (1) RRT1 (quartz arenite micro-facies), (2) RRT2 (quartz wacke) and (3) RRT3 (mudstone micro-facies), (Nabawy et al. 2019).

The quartz arenite micro-facies (RRT1) is composed of ill-sorted, very fine to coarse, angular to subangular quartz grains compacted together and cemented by silica cement with point contact, concavo-convex and suture contacts (Fig. 4c and d). Clay minerals are present as a filling material in the pore spaces and as rims surrounding the grain surfaces (Fig. 4d and e).

The second micro-facies is the quartz wacke (RRT2) which is dominantly distributed in Nubia C. It is represented by fine to medium, moderately hard to friable and slightly pebbly to gravelly cross-laminated to cross-bedded sandstones (Fig. 4b). Petrographically, it is composed of very fine- to coarse-grained, angular to rounded quartz grains cemented by silica cement with some gypsum and a matrix of clay patches that sometimes present as a pore-filling material (15.0–50.0%, Fig. 4f).

The mudstone (siltstone) micro-facies (RRT3) is represented by highly compacted and moderately to well-sorted silt-sized angular quartz grains cemented by clay matrix (> 70%) and some gypsum cement.

Petrographically, the porosity values of both the quartz arenite and quartz wacke micro-facies vary between 15 and 29% with a relatively higher quartz arenite content, while the least porosity values are recognized in the mudstone micro-facies, having less than 10%. The pore spaces of the studied quartz arenite and quartz wacke micro-facies are mostly described as: (1) macro- to mega-intergranular porosity (Fig. 4c, d, e and h), partially reduced by gypsum laminae and well-developed kaolinite booklets (Fig. 4g), and (2) micro-fracture porosity (Fig. 4d), rarely reduced by gypsum laminae (Fig. 4h). The kaolinite clay content is better developed in Nubia C than that of Nubia D giving rise to quartz wacke micro-facies. Further upward, the clay content increases in percentage giving rise to the mudstone micro-facies whereby it forms a good sequence at the top of Nubia C. In addition, the matrix porosity was assigned to the mudstone micro-facies with some micro-intergranular and meso- to macro-channel porosity (Nabawy et al. 2019).

Diagenesis

The diagenetic factors controlling the pore architecture of the studied sequences can be categorized into the two main types provided by Nabway and Kassab (2014): (1) porosity-enhancing factors (dissolution, leaching out and fracturing) and (2) porosity-reducing factors (cementation, compaction and pressure solutions, silicification, authigenic minerals, neo-morphism).

Porosity-Enhancing Diagenetic Factors

Dissolution and leaching out of cement are the most important porosity-enhancing diagenetic processes in the studied Nubia micro-facies. The exceptions are the RRT3 samples near the top of the studied sequence.

The deposition of the Nubia sandstone is characterized by very high intergranular porosity followed by local calcite cementation that prohibited the progress of the overload compaction process and was finally dominated by the severe dissolution of the carbonate cement and the feldspar skeletons due to meteoric water. Exhausted feldspars skeletons are declared from accumulations of authigenic kaolinite booklets that filled the pore spaces (Fig. 4h). The dissolution and leaching-out processes enlarged the fracture system and converted it into a channel system leading to the evolution of more intergranular porosity (Fig. 4f and h) and isolated meso- to mega-vugs (Fig. 4d and g) but rarely to intragranular porosity (Fig. 4e).

The fracture system in the Nubia sequence introduced the main pathways for the invading solutions to dissolve and leach out the dissolved materials whereby a few micro- to meso-fractures are noticed through the matrix and cement of the RRT3 (Fig. 4d and g) and RRT1 samples.

Porosity-Reducing Diagenetic Factors

Overload pressure is an effective porosity-reducing factor that acts as a function in depth. In the study area, mechanical compaction due to tectonic movements is an additional factor supporting the storage capacity reduction (down to 15% in some samples) causing point contacts, suture contacts (Fig. 4c and d), concavo-convex contacts (Fig. 4d), wavy extinction in some quartz grains and fracturing in other quartz grains (Fig. 4c and d).

Silicification is the main porosity-reducing factor that reduces the pore volume and fluid flow capacity through the Nubia sandstone. It is mainly attributed to dissolution and leaching out of silica as well as compaction and pressure solutions that caused the partial dissolution of the quartz grains borders, as is the case in the RRT1 and RRT2 samples of the Naqus Formation (Fig. 4d and f).

Gypsum laminae are also assigned through the Nubia C in the quartz wacke (RRT2) samples, reaching up to 25%. Gypsum is presented with a poikilotopic texture of gypsum cementing the quartz grains to each other and blocking and healing the fractures and the intergranular pores (Fig. 4f and h). In Nubia D, gypsum is considered to be a minor constituent to traces (less than 5%) reducing the pore volume and fractures (Fig. 4c and g).

For the present study, kaolinite is commonly assigned in the Nubia samples as dull patches filling and plugging in some pore spaces to reduce their flow capacity, as is the case in the RRT1 samples (Fig. 4d and g). The percentage of kaolinite increases from the RRT1 samples up to its maximum in the RRT3 samples, whereas the RRT2 samples act as transitional rock types (Fig. 4f and h).

Petrophysical Results

The petrographical and petrophysical properties of the pore and petro-phases of the studied samples are helpful in discriminating them into three reservoir rock types (RRTs). The best petrophysical properties are assigned to the quartz arenite micro-facies (RRT1) for both Nubia C and D ($11.9 \leq \phi_W \leq 24.9\%$, $15.9 \leq \phi_{He} \leq 28.2\%$, $489 \leq k_H \leq 3118$ md, $445 \leq k_{VC} \leq 1876$ md, Table 1). Upward in the studied sequence, Nubia C is further discriminated into two additional rock types (RRT2 quartz wacke and RRT3 mudstone micro-facies, respectively). The lowest petrophysical values and highly anisotropic pore spaces are assigned to the mudstone micro-facies (RRT3) of Nubia C ($1.17 \leq \phi_W \leq 6.06\%$, $6.92 \leq \phi_{He} \leq 12.2\%$, $0.17 \leq k_H \leq 1.67$ md, $0.04 \leq k_{VC} \leq 1.0$ md, Table 1). The r_{35} and r_{dp} pore radii of the studied samples indicate the best pore sizes and fabrics for RRT1 ($9.52 \leq r_{35} \leq 28.9$ μm, $13.9 \leq r_{dp} \leq 37.3$ μm) and the lowest values for RRT3 ($0.13 \leq r_{35} \leq 0.18$ μm, $0.19 \leq r_{dp} \leq 0.46$ μm, Table 1). The RRT1 samples are characterized by a slightly anisotropic pore architecture including electric and permeability anisotropy ($0.85 \leq \lambda_{kC} \leq 1.42$, $0.86 \leq \lambda_{EC} \leq 1.22$, Table 1). On the other side, the RRT3 samples are characterized by more complex pore fabrics and relatively higher anisotropy ($0.54 \leq \lambda_{kC} \leq 2.49$, $0.71 \leq \lambda_{EC} \leq 1.30$, Table 1). In general, the Nubia sandstone pore types are characterized by mostly good to very good connectivity. Finally, a set of statistical models of high reliability are introduced to be applied to further predictions of the petrophysical parameters.

GENERAL DISCUSSION

Impacts of Diagenesis on Pore Fabric and Volume

Impacts of Porosity-Enhancing Factors

Dissolution and leaching out of cement and feldspars increased the channel and intergranular porosity fractions which are the most important types of porosity with the highest contribution to permeability. The highest intergranular porosity is assigned to the quartz arenite micro-facies (RRT1) whereby the highest average helium and water porosity (ϕ_{He}, ϕ_W) and permeability (k) values were assigned to this rock type ($\phi_{He} = 22.7$, $\phi_W = 19.6\%$, while $k_H = 1370$, $k_{VC} = 1062$ md, respectively, Table 1). Micro-fractures played an additional reservoir quality-enhancing role for the Nubia sandstone, wherein they created a subsidiary fracture system in the highly compacted mudstone facies (RRT3) Though it has the least reservoir quality,

some samples have fair porosity and permeability reaching up to 12.2% and 1.67 md, respectively.

Impacts of Porosity-Reducing Factors

Cementation, authigenic minerals and mechanical compaction are the dominant porosity-reducing factors in the Nubia sandstone. Cementation is mostly attributed to silica cement in the form of meniscus cement, which has little to no effect on the final porosity net result in the quartz arenite micro-facies (RRT1). In the present sandstone samples, alteration of feldspars due to chemical reactivity with the invading solutions resulted in the formation of authigenic kaolinite as dispersed clay minerals that filled and lined the pore spaces (Fig. 4d and f). Diagenetic clay minerals are formed as authigenic minerals slightly reducing the average porosity and permeability (ϕ_{He}= 16.2%, k_H = 310 md, Table 1) of the quartz wacke (RRT2) of the Naqus Formation (Fig. 4f) due to the alteration of feldspars into kaolinite booklets filling the pore spaces (Fig. 4h). Therefore, the presence of authigenic kaolinite as dispersed clays filling the pore spaces reduced the permeability from the relatively very high values of RRT1 into the present permeability values of RRT2, which range from good to very good ($26.2 \leq k \leq 1932$ md, Table 1).

Gypsum as a subsidiary cement is an additional slightly reducing cement material filling the pore channels and fractures of the studied rock types, e.g., RRT1 (Fig. 4g). The reducing impacts of gypsum increase, as is the case in the RRT2 samples (quartz wacke micro-facies) whereby gypsum changed from a pore-filling fabric (Fig. 4h) to a poikilotopic fabric.

The mechanical compaction due to overload pressure is an additional reducing effect which seems to have a little or negligible effect on the reservoir quality of the RRT1 samples. This pressure compaction is presented by the alignment of the quartz grains as point contact fabrics, sometimes by suture and concavo-convex contact fabrics (Fig. 4d and e).

Impacts of Pore Size on Accessible Pore Volume

Plotting the bulk density as a function of porosity that was measured using water and helium injection (ϕ_W, ϕ_{He}, Fig. 5) may be applied as a quality control (QC) for the processed data before further processing and modeling. In addition, a greater difference between the two values (ϕ_W, ϕ_{He}) indicates the presence of micro- and nano-pore sizes and cement control on the pore diameters, which become smaller and narrower so as to be accessible by water injection (El Sharawy and Nabawy 2016b, 2018; Kassab et al. 2017). The relatively high coefficient of determination values ($0.938 \geq R^2 \geq 0.788$, Fig. 5) for the different rock types indicate the reliability and consistency of the measured data and the suitability for further statistical processing. The average inaccessible porosity values (ϕ_{inacc}, %) are high for the relatively poor porous samples (RRT3) reaching up to 64.7%, whereas they are lowest (13.7%) for the highly porous samples, RRT1 (Table 1).

Contribution of Porosity (ϕ) to Permeability (k)

Presenting permeability as a function of water and helium porosity is not always systematic, and the output factors of the final model may be a good indication for the pore types and pore throat properties. The relatively high difference between the water and helium porosity caused a relatively high shift of the best-fit line of the permeability–porosity relationship in the RRT3 samples and less so in the RRT2 samples (Fig. 6a). The micro- and nano-sizes of the pore spaces reduce the reliability of the relationships with the water porosity ($R^2 \leq 0.643$). In the case of the RRT1 samples, the presence of different pore sizes reduces the reliability of this relationship not being accepted ($R^2 \leq 0.36$). This indicates the necessity for further discrimination of these samples into further subgroups: RRT1* belonging to Nubia D and RRT1 belonging to Nubia C (Fig. 6b). This further grouping enhanced the reliability of the porosity–permeability relationship. One of these groups is characterized by relatively lower porosity values but with the same permeability contribution, i.e., much better fluid-conductor pore types, intergranular and fracture porosity (Fig. 4d and h).

The mudstone ϕ_W–k relationship seems to be much less reliable than the other relationship. This could be explained by the lesser accessibility of water in the micropore spaces and matrix porosity in addition to the swelling effects of the clay minerals in contact with the invading water, i.e., to block and isolate some pore spaces causing much less porosity and disturbed relationships. The reliability of the obtained model may introduce it as a successful model applicable to more extended sandstone sequences.

Table 1. Pore and petro-phase storage and flow capacities, electric properties and reservoir quality parameters of the studied micro-facies in the Gebel El-Zeit area

Lithology	N	ρ_g (g/cm³)	ρ_b (g/cm³)	ϕ_{He} (%)	ϕ_W (%)	ϕ_{inacc} (%)	k_H (md)	k_{VC} (md)	FR_{TH}	FR_{TVC}	λ_{kC}	λ_{EC}	a	m	r_{35} (μm)	r_{dp} (μm)
RRT1 (Quartz Arenite)	Min	2.51	1.84	15.9	11.9	5.29	489	445	22.23	26.23	0.85	0.86	0.98–1.02	2.15–2.33	9.52	13.9
	Average	2.59	2.00	22.7	19.6	13.7	1370	1062	41.52	39.77	1.12	1.02			17.9	23.1
	Max	2.68	2.24	28.2	24.9	25.2	3118	1876	77.22	68.67	1.42	1.22			28.9	37.3
RRT2 (Quartz Wacke)	Min	2.30	2.09	14.1	9.06	11.5	26.2	32.40	39.41	13.24	0.59	0.89	1.05	2.00	2.38	3.28
	Average	2.60	2.18	16.2	12.1	25.5	310	291	80.68	25.41	1.05	1.20			4.25	6.69
	Max	2.64	2.26	20.2	16.5	38.3	965	1932	147.6	38.93	1.58	1.50			7.86	15.3
RRT3 (Mudstone)	Min	2.60	2.32	6.92	1.17	42.3	0.17	0.04	22.30	17.65	0.54	0.71	0.21	2.04	0.13	0.19
	Average	2.63	2.39	9.25	3.36	64.7	0.63	0.39	112.9	157.7	1.55	0.98			0.16	0.28
	Max	2.66	2.45	12.2	6.06	83.3	1.67	1.00	317.7	467.9	2.49	1.30			0.18	0.46

where ρ_g and ρ_b are the bulk and grain densities, respectively; ϕ_{He} and ϕ_W are the porosity values measured by both the helium and water injection techniques; ϕ_{inacc} is the inaccessible porosity for water injection; k_H and k_{VC} are the horizontal permeability and the corrected permeability in the vertical direction, respectively; FR_{TH} and FR_{TVC} are the true formation resistivity factors in the horizontal direction and the corrected true formation resistivity factor in the vertical direction, respectively; λ_{kC} and λ_{EC} are the corrected permeability and electric anisotropies, respectively; a and m are Archie's parameters for each rock type, respectively; r_{35} is the pore radius introduced by Winland (1972) that corresponds to 35% mercury saturation; and r_{dp} is the pore radius corresponding to the displacement pressure as described by Schowalter (1979)
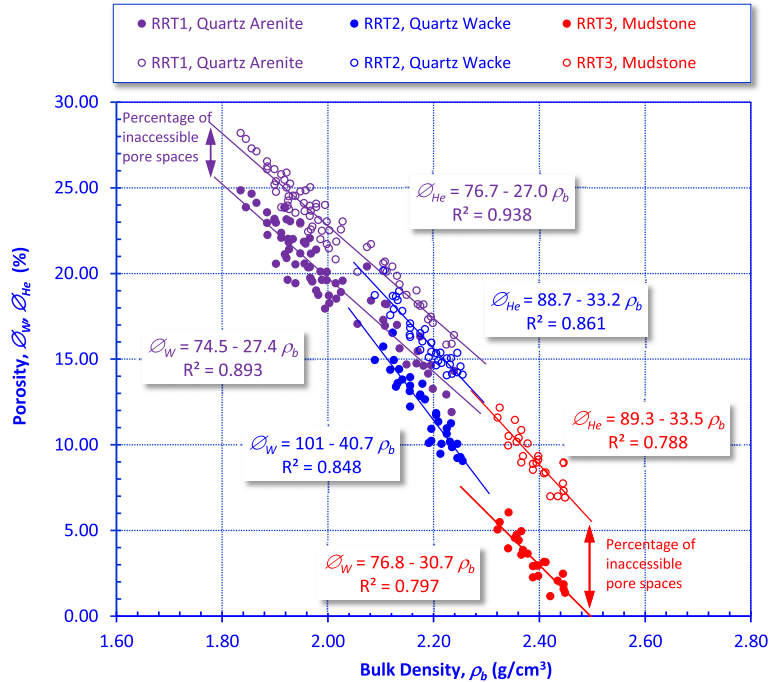
Fig. 5. Plot showing the bulk density (ρ_b) vs. porosity measured by two techniques, helium (ϕ_{He}, open circles) and water injection (ϕ_W, solid circles). Negative correlations were encountered between the bulk density and both the helium and water porosity. The helium porosity values are always greater than the water porosity values whereby the difference represents percentage of nano- and micropore volumes that the water cannot invade them. Annotation: $n = 72$ samples for RRT1, 34 samples for RRT2 and 24 samples for RRT3.

Impacts of Fractures on Permeability Anisotropy

Plotting the vertical permeability value of the given rock samples as a function of the horizontal permeability is a good indication of the presence of vertical micro-fractures. These micro-fractures are the main contributors to increase in the vertical permeability rather than the horizontal one (Meyer and Krause 2006; Nabawy and Barakat 2017). On the other side, rock samples with primary depositional fabrics are characterized by higher horizontal permeability values than vertical ones (Nabawy and Al-Azazi 2015; Nabawy and Géraud 2016; Veloso et al. 2016). For the present study, plotting the vertical permeability as a function of the horizontal one indicates that the mudstone facies (RRT3) are composed of depositional fabrics ($k_H > k_V$, Fig. 7a), whereas RRT2 samples are mostly characterized by the presence of some subsidiary vertical micro-fractures ($k_V > k_H$, Fig. 7a). This vertical permeability can be calculated in terms of the horizontal permeability by using the following model:

$$k_V = 0.56\, k_H^{1.06} \quad \left(R^2 = 0.982\right) \qquad (8)$$

The multiplication factor and exponent of this reliable relationship indicate that most of the studied samples are characterized by depositional fabrics whereby $k_H > k_V$ for most of the studied samples (Fig. 7a).

For the RRT1 samples, the fabrics are mixed between the primary depositional and secondary fabrics. Differentiating the RRT1 samples into two subgroups indicates that some RRT1 Nubia C samples are characterized by secondary fabrics, whereas the other group of Nubia D samples are characterized by depositional fabrics (Fig. 7b).

Impacts of Mineral Composition on FR$_T$ and Archie's Parameters

The true formation resistivity factor (FR$_T$) of the studied clastic samples is mostly controlled by
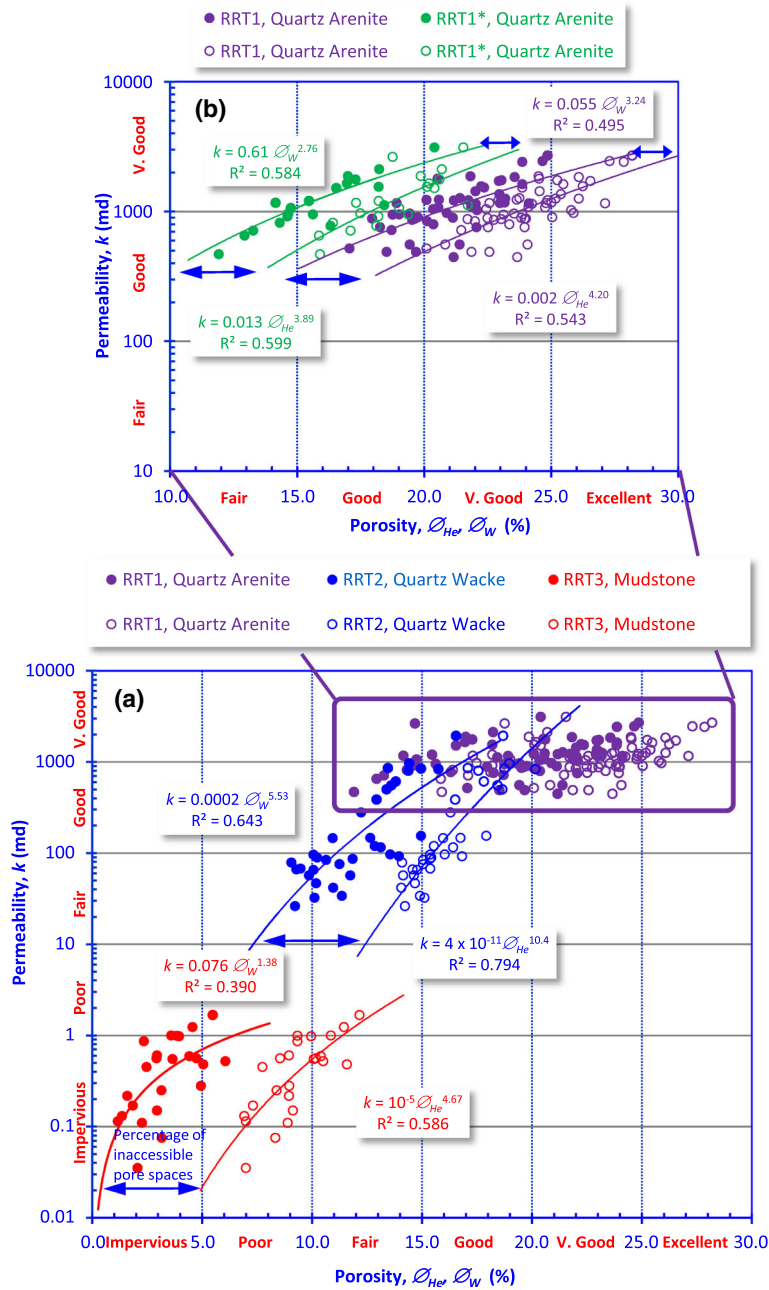
Fig. 6. Plot showing permeability as a function of porosity measured by (**a**) helium (ϕ_{He}, open circles) and (**b**) water injection (ϕ_W, closed circles). Direct proportional relationships were encountered between permeability and porosity. Note that the determination coefficients of the relationships of permeability with the helium porosity are higher than those with the water porosity. Annotation: (**a**) $n = 72$ samples for RRT1, 34 samples for RRT2 and 24 samples for RRT3; (**b**) $n = 24$ samples for RRT1* and 48 samples for RRT1.

the mineral composition, the presence of fine electric conductors (clays and iron oxides), pore volume and pore connectivity. The quartz arenite samples (RRT1) of both the Araba and Naqus Formations are characterized by very low values (FR$_T$ ≤ 50.0), (Nabawy et al. 2015), whereas the FR$_T$ values of the
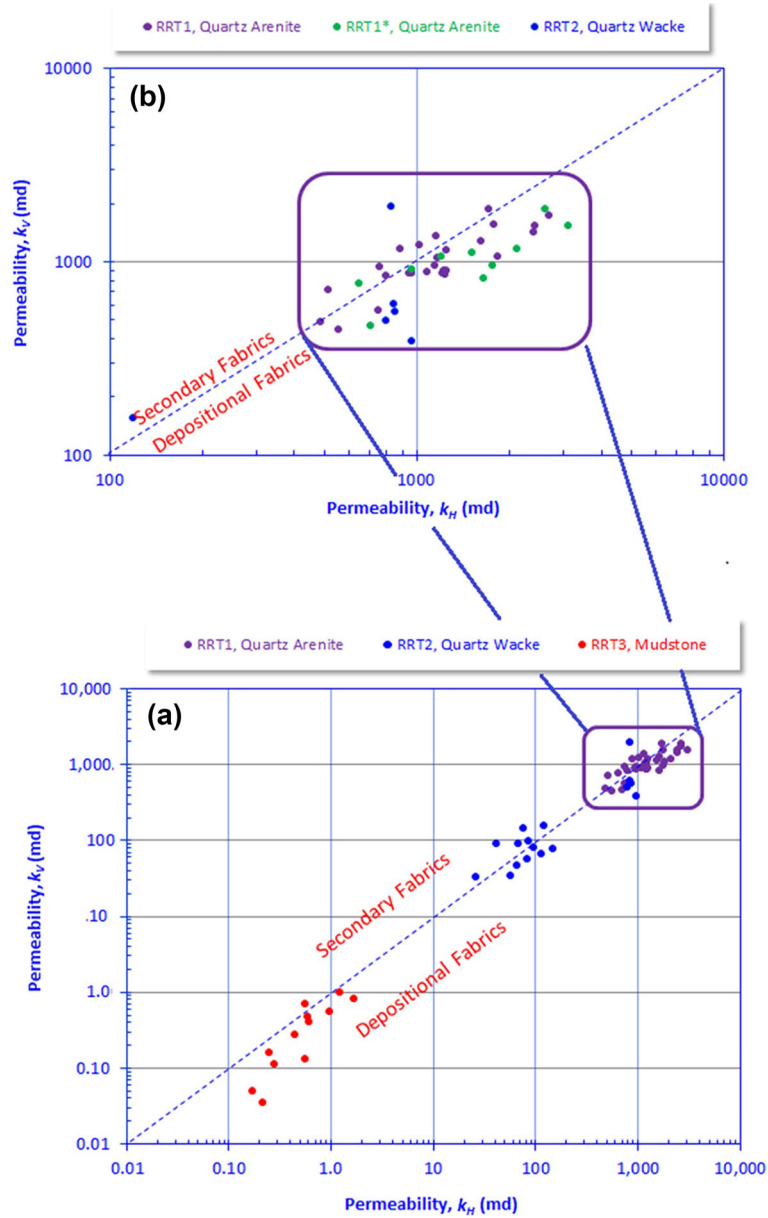
Fig. 7. Log–log plot showing vertical permeability values as a function of horizontal permeability of the studied samples. Annotations: (**a**) $n =36$ samples for RRT1, 17 samples for RRT2, and 12 samples for RRT3. (**b**) $n =12$ samples for RRT1*, five samples for RRT2 and 24 samples for RRT1.

mudstone facies have relatively scattered values ranging from low to very high ($50.0 \leq FR_T \leq 500.0$, Table 1). The relatively high FR_T values of some RRT4 samples may be attributed to the relatively poor porosity values ($\phi_W \leq 6.06\%$) and the silt-sized quartz grains and gypsum flakes rather than the presence of clay minerals (Fig. 4g) which are present in other samples of low FR_T values.

Plotting the true formation resistivity factor (FR_T) as a function of water porosity (ϕ_W) enables modeling the interrelationship and estimation of Archie's parameters including the lithology factor (a) and porosity exponent (m) (Fig. 8). The values of Archie's equation indicate values more or less consistent with the m values through the different rock types approaches ($2.00 \leq m \leq 2.33$, Fig. 8). The
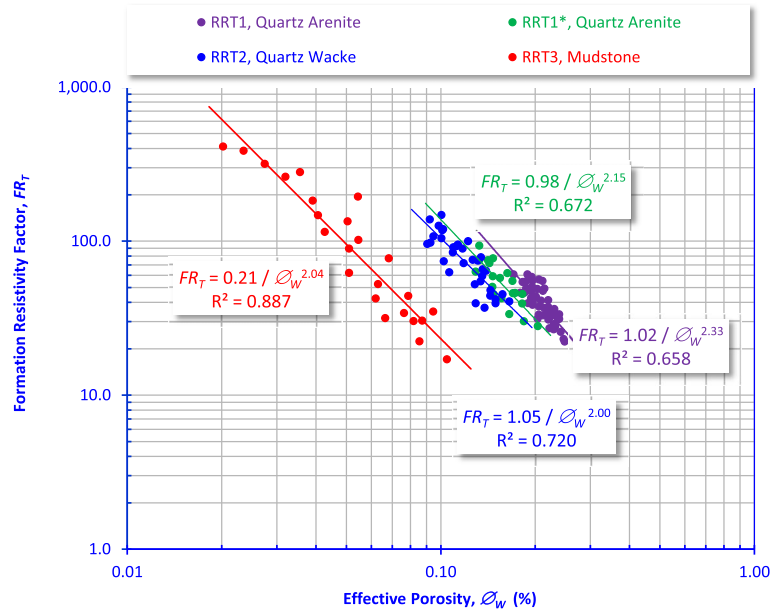
Fig. 8. Log–log graph showing true formation resistivity factor (FR_T) of the studied rock types as a function of porosity that was measured by using water injection (ϕ_W). Annotation: $n = 48$ samples for RRT1, 24 samples for RRT1*, 34 samples for RRT2 and 24 samples for RRT3.

values of the lithology factor show some differences from one rock type to another. The least value is assigned to the RRT3 mudstone samples ($a = 0.21$), and the highest values (1.02) are assigned to the quartz arenite of Nubia C. These values are consistent with extant literatures that refer to m equaling 2.0 as is the case in the intergranular porosity of sandstone (Focke and Munn 1987; El Sharawy and Nabawy 2018). The values of the lithology factor a are also consistent with the extent literatures which state that the low values of the lithology factor refer to fine clastics (mudstone and wackestone), whereas the higher values (≈ 1) are assigned to quartz arenites (Archie 1942, 1952; Nabawy et al. 2015; El Sharawy and Nabawy 2016b, 2018).

Impacts of Fractures on FR_T

Plotting the values of the vertical true formation resistivity factor FR_T as a function of the horizontal values may be a good indication of the 3D distribution of the authigenic clay minerals and fine conductive minerals (iron oxides) as well as of the presence of vertical micro-fractures (Nabawy and Barakat 2017; Nabawy et al. 2018). Rock samples with primary depositional fabrics are characterized by higher FR_{TV} values than horizontal ones (Nabawy and Al-Azazi 2015; Nabawy and Géraud 2016; Veloso et al. 2016). For the present study, plotting the vertical true formation factor as a function of the horizontal one indicates that most of the studied samples are characterized by secondary electric fabrics ($FR_{TH} > FR_{TV}$, Fig. 9). These secondary fabrics indicate that the pore connectivity in the vertical directions is much better than that in the horizontal directions due to the circulations of the dissolving solutions. This enhanced the micro-fractures or filled them with authigenic conductive clay minerals which may reduce the permeability but act as electric conductive bridges between the pore spaces in the vertical directions. However, few RRT3 mudstone samples are still characterized by highly anisotropic electric depositional fabrics due to lamination with fine electric conductors (Fig. 9).

Impacts of the Effective Pore Radii (r_{35} and r_{dp}) on FR_T

The electric resistivity is mostly controlled by the conductive saline fluids inside the pore spaces and on the fine conductors as subsidiary conductors. Similar to permeability, the FR_T as an indicator
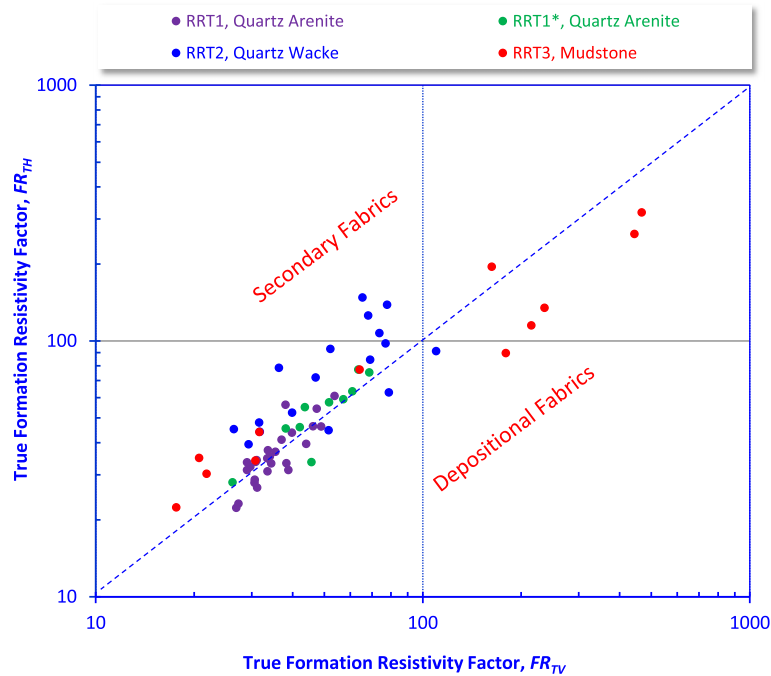
Fig. 9. Log–log plot showing vertical true formation resistivity factor as a function of horizontal true formation resistivity of the studied samples. Annotation: $n = 24$ samples for RRT1, 12 samples for RRT1*, 17 samples for RRT2 and 12 samples for RRT3.

parameter for electric resistivity is mostly controlled by the pore radii of the studied rocks. Therefore, plotting the FR_T as a function of r_{35} and r_{dp} indicates inversely proportional relationships with the highest reliability assigned to the Nubia D quartz arenite (RRT1*) and the lowest reliability assigned to that of Nubia C (RRT1) (Fig. 10). This can be attributed to the micro- and nano-pore throat sizes of the Nubia C samples. However, the reliability of the relationships obtained from plotting r_{35} and r_{dp} with FR_T values is very good to excellent ($R^2 \geq 0.667$). The authigenic clay content acts like fine electric conductors during the electric measurements which supports the electric flow and therefore reduces the FR_T values but does not reduce or block the pore throats (Nabawy 2014).

Pore Fabric Anisotropy

The pore fabric in the present study refers to the anisotropy of the pore spaces. It is responsible for both the hydraulic conductivity (permeability) anisotropy and the electric resistivity (formation resistivity factor) anisotropy. The hydraulic and electric anisotropy can be calculated as the square root of the ratio of the property value in the horizontal direction to the same property value in the vertical direction. The primary depositional fabrics (flattened pore spaces) are characterized by $k_H \geq k_V$ (Fig. 7) and $FR_{TH} \leq FR_{TV}$ (Fig. 9), whereas the secondary fabrics (elongated pore spaces due to tectonics and fracturing) are characterized by $k_H \leq k_V$ (Fig. 7) and $FR_{TH} \geq FR_{TV}$ (Fig. 9). The reliability of the obtained models is accepted with $0.661 \geq R^2 \geq 0.475$, and most of the samples are scattered along the symmetry line with a slight shift toward the depositional fabrics and scattering of the mudstone samples (Fig. 9).

Plotting the hydraulic anisotropy (λ_k) as a function of the electric anisotropy (λ_E) indicates that the presence of different pore throat sizes is more effective in the case of hydraulic anisotropy rather than in the electric one with a shift of sample data toward the λ_k axis (Fig. 11). Electrically, the studied samples are characterized by slightly anisotropic to isotropic fabrics with many samples having $\lambda_E < 1.0$, i.e., secondary fabrics and $FR_{TH} \geq FR_{TV}$. The hydraulic anisotropy is also characterized by slightly anisotropic to isotropic fabrics. However, some
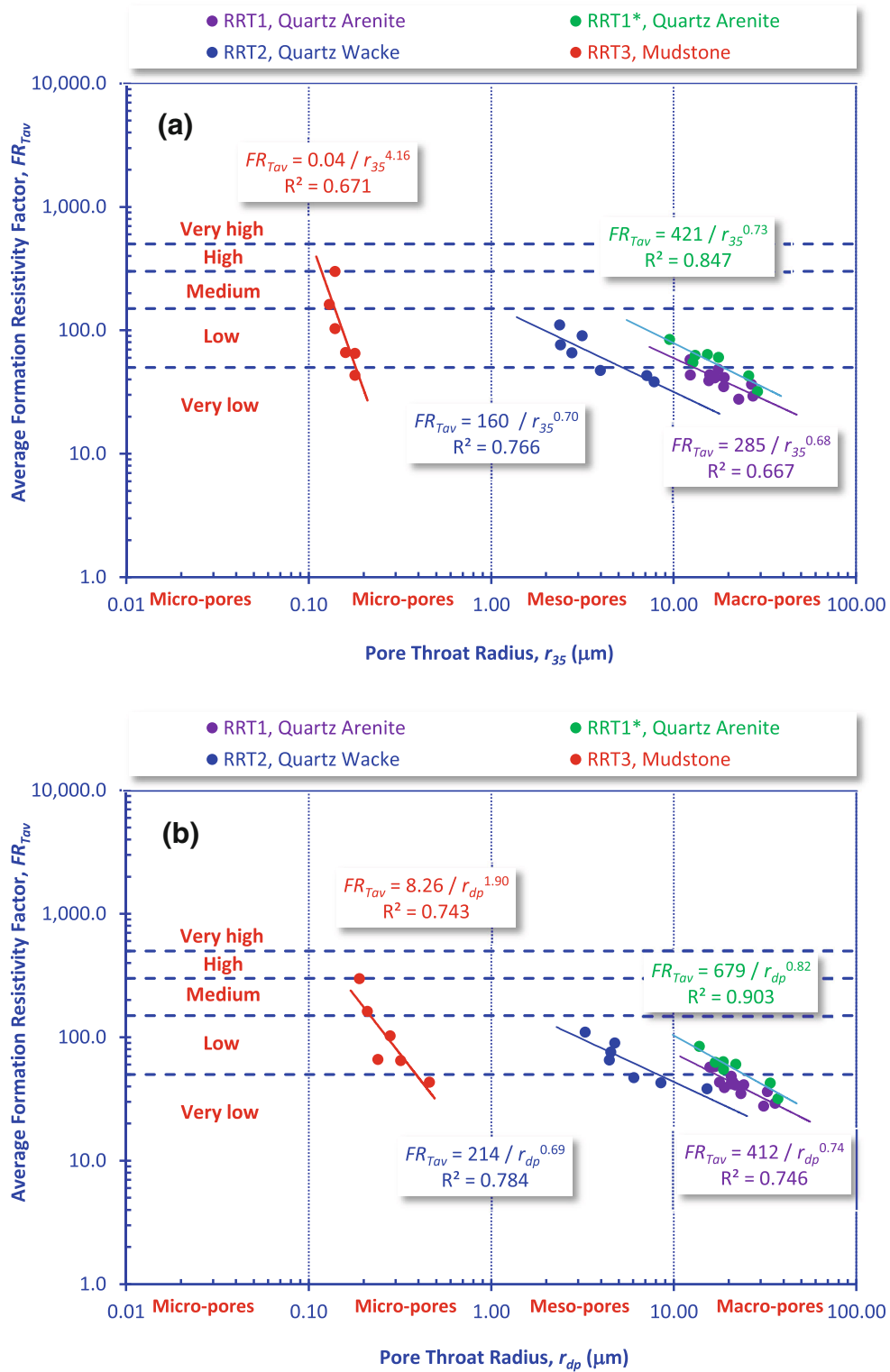
Fig. 10. Log–log plot showing formation resistivity factor as a function of pore throat radius of: (**a**) r_{35} of Winland (1972) and (**b**) r_{dp} of Pittman (1992). Annotation: n =12 samples for RRT1, n =8 samples for RRT1*, 7 samples for RRT2 and 6 samples for RRT3.
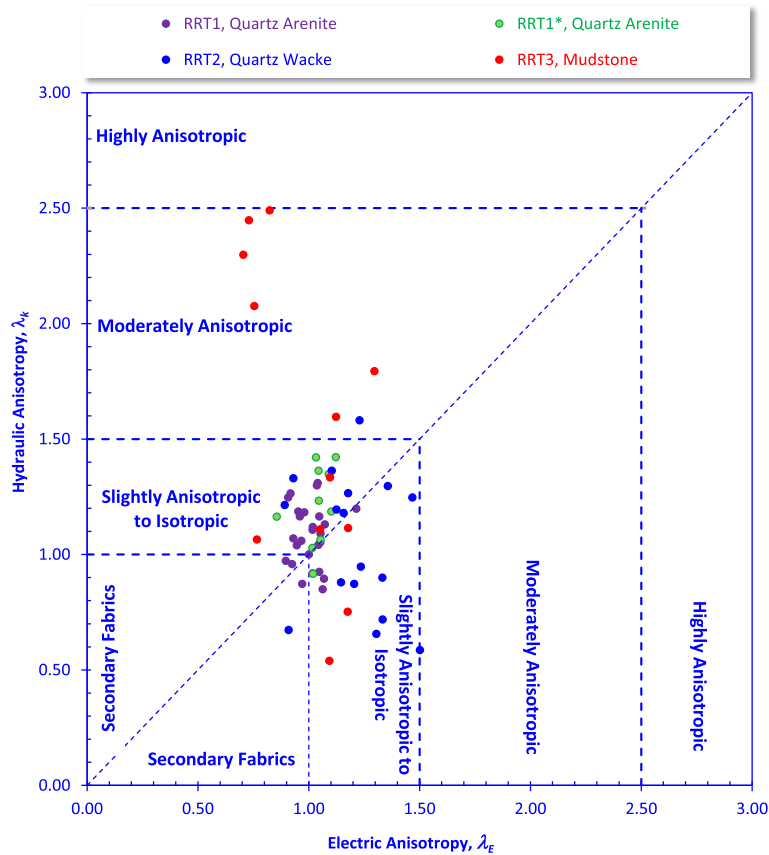
Fig. 11. Plot showing hydraulic anisotropy as a function of electric anisotropy. Classification and ranking follow Nabawy et al. (2015). Annotation: n =24 samples for RRT1, 12 samples for RRT1*, 17 samples for RRT2 and 12 samples for RRT3.

samples (RRT4) are moderately anisotropic ($2.5 \geq \lambda_k \geq 1.5$), while others are characterized by $\lambda_k < 1.0$ (Fig. 11). However, this slight difference in behavior between λ_k and λ_E can be attributed to the effect of the clay content, type and distribution, i.e., the hydraulic and electric effect of the clay content.

Reservoir Quality Assessment

The reservoir quality assessment is based on many parameters that describe and characterize the ability of rocks to store and transmit fluids. Therefore, plotting the measured pore volume, pore transmissivity and anisotropy as a function of depth is a helpful procedure for describing and qualifying the reservoir rocks. For the present outcrop sequence, as analogous to the subsurface reservoir rocks in the Gulf of Suez, porosity (water and helium porosity), permeability (vertical and horizontal

permeability), true formation resistivity factors (vertical and horizontal formation resistivity factors) and pore anisotropy (electric and fluid flow anisotropy) are plotted vs. depth (Fig. 12). In this plot, the 10% porosity and 1 md cutoff value are applied to indicate the most prospective horizons. This indicates two nonporous and nonpermeable flow units of micro- to nano-pore throat sizes at heights of 40–85 and 245–280 m through the Nubia C. The consistent differences between the water and helium porosity increase through these two flow units, supporting the presence of complex pore spaces through these units which are composed mostly of RRT3 mudstone samples. Plotting both the permeability and formation resistivity factors in both the vertical and horizontal directions indicates the presence of some horizons characterized by subsidiary micro-fracture system ($k_V > k_H$, $FR_{TH} > FR_{TV}$, green shadow, Fig. 12). The subsidiary micro-fracture system can be detected using FR_T logs rather than k
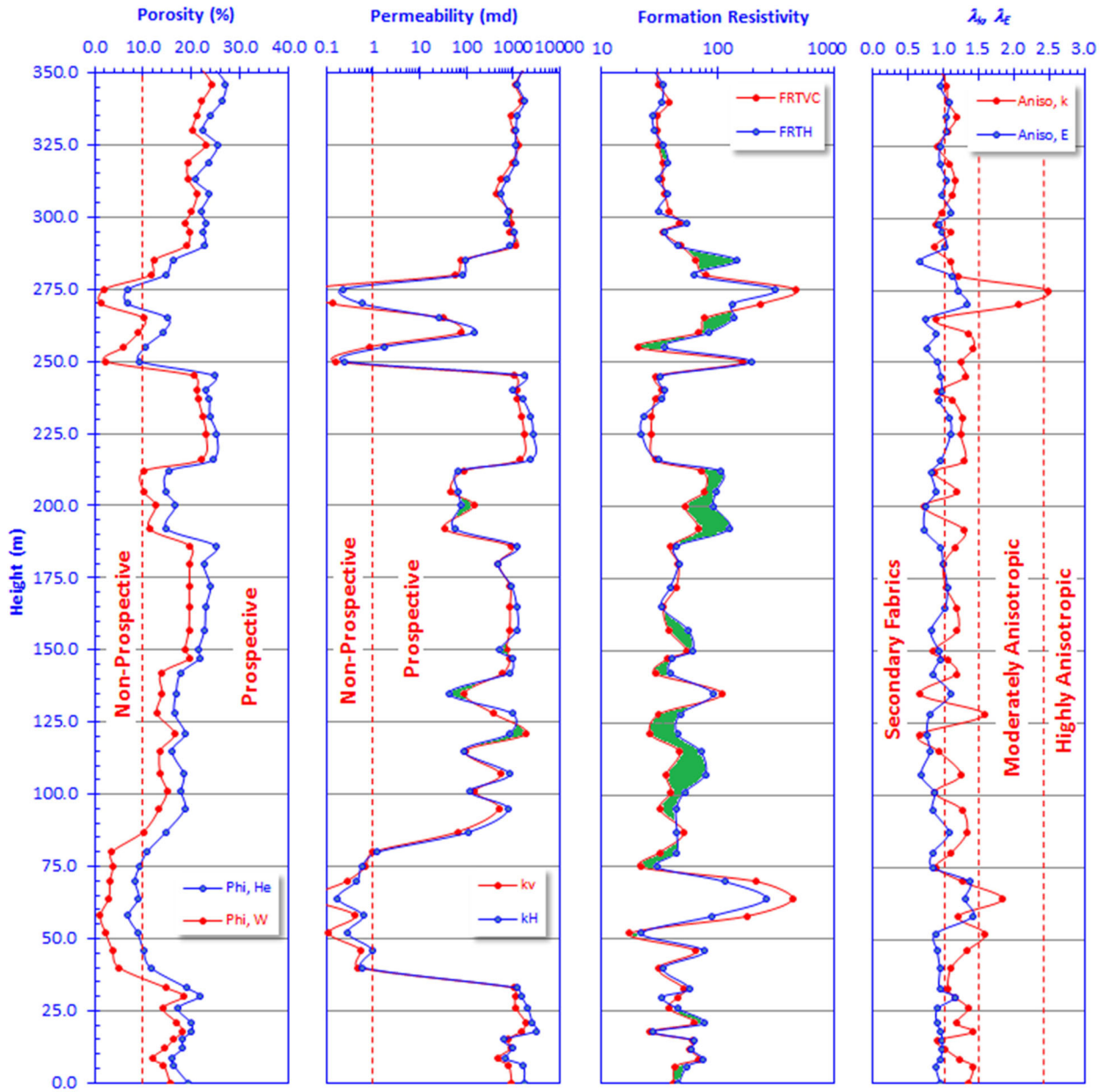
Fig. 12. Plot showing petrophysical and reservoir quality parameters as a function of height for the Nubia sandstone in the studied area. Green shades indicate the presence of a micro-fracture system. The helium and water porosities were plotted in the first track (first track to the left) with cutoff value (porosity = 10%); vertical and horizontal permeabilities were plotted in the second track with cutoff value (permeability = 1 md); vertical and horizontal formation resistivity factors were plotted in the third track; and finally, both the electric and permeability anisotropies were plotted in the last track (secondary fabrics means $\lambda < 1$, for isotropic and slightly anisotropic fabrics $1 < \lambda < 1.5$, for moderately anisotropic fabrics $1.5 < \lambda < 2.5$ and for highly anisotropic fabrics $2.5 < \lambda$). Samples are considered nonprospective for hydrocarbon accumulations in their subsurface extensions when they have porosity $< 10\%$ and permeability < 1 md.

logs. This can be explained by the presence of different dominant and subsidiary pore sizes due to the presence of the subsidiary vertical micro-fracture system which may be attenuated later by the authi-genic clay minerals (fine electric conductors) as a filling material which slightly reduces the vertical fluid flow but does not stop the vertical electric flow; i.e., it supports the pore anisotropy in the vertical

direction (Fig. 12). This complex pore fabric could be seen from the inconsistency between the electric and permeability anisotropy (λ_k, λ_E, Fig. 12, track 4). The micro-fracture system is also indicated by shifting the anisotropy parameters to less than 1.00 with a greater number of shifts of the electric anisotropy toward the left. The anisotropy is mostly slight (λ_k, $\lambda_E \leq 1.5$). Some flow units are characterized by permeability anisotropy that has shifted to the moderate anisotropy rank. These flow units are characterized by low porosity and permeability values and relatively high FR_T values due to the cementing of the vertical system by silica cement material rather than being filled with clay minerals; i.e., both the permeability and FR_T values were greatly reduced.

CONCLUSIONS

The Nubia sandstone sequence along the southwest Gulf of Suez can be classified into Nubia C and D (355 m thickness) which are described as quartz arenite (RRT1), quartz wacke (RRT2) and mudstone samples (RRT3). The RRT1 samples have the best average storage capacities, flow capacities and effective pore throat radii as well as slight pore anisotropy (ϕ_{He}= 22.7%, ϕ_W= 19.6%, k_H = 1370 md, k_{VC} = 1062 md). On the other hand, the RRT3 samples have the least reservoir quality (ϕ_{He}= 9.25%, ϕ_W= 3.36%, k_H = 0.63 md, $\leq k_{VC}$ = 0.69 md). The anisotropy of pore spaces was estimated by measuring the permeability and formation resistivity factors in the vertical and horizontal directions (to estimate the pore anisotropy) and by measuring the effective pore radii of Winland (r_{35}) and the displacement pressure (r_{dp}). The pore architecture of the RRT1 samples has the highest pore radius and the lowest anisotropy (r_{35} = 17.9 μm, r_{dp} = 23.1 μm, λ_{kC}= 1.12, λ_{EC}= 1.02), whereas it is narrower and more complicated for the RRT3 mudstone samples (r_{35} = 0.16 μm, r_{dp} = 0.28 μm, λ_{kC}= 1.55, λ_{EC}= 0.98).

The presence of micro- and nano-pore sizes in the studied pore spaces is mostly attributed to the presence of some micro-fractures in the vertical direction ($k_V > k_H$, $FR_{TH} > FR_{TV}$). This system was healed by silica cement for the RRT3 samples causing moderate anisotropy by reducing the permeability greatly in the vertical direction and subsequently causing very high FR_{TV} values. On the other hand, for the RRT2 samples, impact of this fracture system was reduced due to filling by kaolinite clay mineral. This reduced the permeability but did not increase the FR_{TV} values due to the electric activity of the clay content.

REFERENCES

Abdallah, A. M., & Adindani, A. (1963). *Stratigraphy of Upper Paleozoic rocks, western side of the Gulf of Suez* (Vol. 25). Egypt: Geological Survey and Mineral Resource Department.

Abdallah, A. M., Darwish, M., El Aref, M., & Helba, A. A. (1992a). Lithostratigraphy of the pre-Cenomanian clastics of north Wadi Qena, Eastern Desert, Egypt. In A. Sadek (Ed.), *Proceedings of the first international conference on Geology of the Arab World* (pp. 255–282). Cairo: Cairo University.

Abdallah, A. M., El Aref, M. M., & Helba, A. A. (1992b). Lithostratigraphy of the pre-Cenomanian clastics of north Wadi Qena, Eastern Desert, Egypt. In Proceedings of the second international conference on Geology of the Arab World (pp. 255–282). Cairo University, Cairo.

Abdel-Wahab, A. A. (1988). Lithofacies and diagenesis of the Nubia Formation at Central Eastern Desert, Egypt. In *9th EGPC Expl. Conf.*, Cairo, 9.

Abdel-Wahab, A. A. (1998). Diagenetic history of Cambrian quartz arenite, Ras Dib-Zeit Bay area, Gulf of Suez, Eastern Desert, Egypt. *Sedimentary Geology, 121*(1), 121–140.

Aboud, E., Salem, A., & Ushijima, K. (2005). Subsurface structural mapping of Gebel El-Zeit area, Gulf of Suez, Egypt; using aeromagnetic data. *Earth Planets Space, 57,* 755–760.

Allam, A. (1988). Geological and structural study on Gebel El-Zeit area. *Journal of African Earth Sciences, 7*(7–8), 933–944.

Allam, A. (1989). Paleozoic sandstones in Wadi Feiran-El Tor area, Sinai, Egypt. *Journal of African Earth Sciences, 9,* 49–57.

Angelier, J. (1985). Extension and rifting, the Zeit region, Gulf of Suez. *Journal of Structural Geology, 7,* 605–612.

Antonellini, M., Aydin, A., Pollard, D. D., & d'Onfro, P. (1994). Petrophysical study of faults in sandstone using petrographic image analysis and X-ray computerized tomography. *Pure and Applied Geophysics, 143*(1–3), 181–201.

A Surface Outcrop Analog

Archie, G. E. (1942). The electrical resistivity log as an aid in determining some reservoir characteristics. *Petroleum Transactions of AIME, 146,* 54–62.

Archie, G. E. (1952). Classification of carbonate reservoir rocks and petrophysical considerations. *AAPG Bulletin, 36*(2), 218–298.

Beleity, A. M, Ghoneim, M., Hinawi, M., Fathi, M., Gebali, H., & Kamel, M. (1986). Paleozoic and stratigraphy, paleogeography and paleotectonics in the Gulf of Suez. In: 8th EGPC Expl. Conf. Cairo, pp. 17–23.

Benson, P. M., Meredith, P. G., & Platzman, E. S. (2003). Relating pore fabric geometry to acoustic and permeability anisotropy in Crab Orchard Sandstone: A laboratory study using magnetic ferrofluid. *Geophysical Research Letters, 30*(19), 1–4.

Borradaile, G., & Jackson, M. (2004). Anisotropy of magnetic susceptibility (AMS): Magnetic petrofabrics of deformed rocks. *Geological Society London Special Publications, 238*(1), 299–360.

Bubeck, A., Walker, R. J., Healy, D., Dobbs, M., & Holwell, D. A. (2017). Pore geometry as a control on rock strength. *Earth and Planetary Science Letters, 457,* 38–48.

Caine, J. S., Evans, J. P., & Forster, C. B. (1996). Fault zone architecture and permeability structure. *Geology, 24,* 1025–1028.

Colletta, B., Moretti, I., Chenet, P. Y., & Muller, C. (1986). The structure of the Gebel Zeit area: A field example of tilted block crest in the Suez rift. Institute Francais du petrole, Compagnie Francaise des petroles, Ref. IFP 34547.

David, C., Bertauld, D., Dautriat, J., Sarout, J., Menéndez, B., & Nabawy, B. S. (2015). Detection of moving capillary front in porous rocks using X-ray and ultrasonic methods. *Frontiers in Physics, 3*(53), 1–14.

David, C., Wong, T., Zhu, W., & Zhang, J. (1994). Laboratory measurements of compaction induced permeability change in porous rocks: Implications for the generation and maintenance of pore pressure excess in the crust PAGEOPH, 142.

EGPC, Egyptian General Petroleum Corporation. (1996). Gulf of Suez oil fields: A comprehensive overview, 736 p.

Ehrlich, R., Crabtree, S. J., Kennedy, S. K., & Cannon, R. L. (1984). Petrographic image analysis: I. Analysis of reservoir pore complexes. *Journal of Sedimentary Research, 54*(4), 1365–1378.

El Sharawy, M. S., & Nabawy, B. S. (2016a). Determination of electrofacies using wireline logs based on multivariate statistical analysis for the Kareem Formation, Gulf of Suez, Egypt. *Environmental Earth, 75*(21), Article 1394.

El Sharawy, M. S., & Nabawy, B. S. (2016b). Geological and petrophysical characterization of the lower Senonian Matulla Formation in Southern and Central Gulf of Suez, Egypt. *Arabian Journal for Science and Engineering, 41*(1), 281–300.

El Sharawy, M. S., & Nabawy, B. S. (2018). Determining the porosity exponent m and lithology factor for sandstones and their control by overburden pressure: A case study from the Gulf of Suez, Egypt. *AAPG Bulletin, 102*(9), 1893–1910.

El-Gindi, A. W. (1972). *Tectonics and facies changes in the Gebel El-Zeit area.* M.Sc. Thesis, Fac. Sci. Cairo Univ., Egypt, 110.

Ellis, M. H., Sinha, M. C., Minshull, T. A., Sothcott, J., & Best, A. I. (2010). An anisotropic model for the electrical resistivity of two-phase geologic materials. *Geophysics, 75*(6), E161–E170.

Etris, E. L., Brumfield, D. S., & Ehrlich, R. (1988). Relations between pores, throats and permeability: A petrographic/physical analysis of some carbonate grainstones and packstones. *Carbonates and Evaporites, 3*(1), 17–32.

Farouk, A. M. (1965). *Geophysical studies on the area between Wadi Dara and Gebel El-Zeit, Gulf of Suez district, U.A.R. for petroleum Exploration.* Assiut University, Unpublished M.Sc. Thesis.

Farrell, N. J. C., & Healy, D. (2017). Anisotropic pore fabrics in faulted porous sandstones. *Journal of Structural Geology, 104,* 125–141.

Farrell, N. J. C., Healy, D., & Taylor, C. W. (2014). Anisotropy of permeability in faulted porous sandstones. *Journal of Structural Geology, 63,* 50–67.

Focke, J. W., & Munn, D. (1987). Cementation exponents in Middle Eastern carbonate reservoir. *SPE Formation Evaluation, 2*(2), 155–167.

Guo, X., Yoshino, T., & Katayama, I. (2011). Electrical conductivity anisotropy of deformed talc rocks and serpentinites at 3 GPa. *Physics of the Earth and Planetary Interiors, 188*(1–2), 69–81.

Hagras, M. (1986). Some geological observations in the Gulf of Suez. In *8th EGPC Expl. Conf.*, Cairo, Egypt, Vol. 1, pp 53–73.

Hassan, A. A. (1967). A new Carboniferous occurrence in Abu Durba, Sinai, Egypt. In *6th Arab petroleum Congress*, Vol. 2, pp. 1–8.

Healy, D. (2012). Anisotropic poroelasticity and the response of faulted rock to changes in pore-fluid pressure. *Geological Society of London, Special Publications, 367,* 201–214.

Ibrahim, A. A. (1996). *Petroleum geology of the Cretaceous and pre-Cretaceous sediments in some oil fields in the Gulf of Suez area, Egypt.* Unpublished Ph.D. Thesis, Cairo Univ., 211.

Issawi, B., El-Hinnawi, M., Francis, M., & Mazhar, A. (1999). The Phanerozoic geology of Egypt, a geodynamic approach. *Egyptian Geological Survey & Mining Authority, Special publication, 76,* 462.

Issawi, B., & Jux, U. (1982). Contributions to the stratigraphy of the Paleozoic rocks in Egypt. *Geological Survey of Egypt, 64,* 1–28.

Jackson, J. A., White, N. J., Garfunkel, Z., & Anderson, H. (1988). Relations between normal-fault geometry, tilting and vertical motions in extensional terrains: An example from the southern Gulf of Suez. *Journal of Structural Geology, 10,* 155–170.

Jayangondaperumal, R., Dubey, A. K., Kumar, B. S., Wesnousky, S. K., & Sangode, S. J. (2010). Magnetic fabrics indicating Late Quaternary seismicity in the Himalayan foothills. *International Journal of Earth Sciences, 99,* S265–S278.

Jelinek, V. (1981). Characterization of the magnetic fabrics of rocks. *Tectonophysics, 79,* T63–T67.

Kassab, M. A. M., Abu Hashish, M., Nabawy, B. S., & El-Nagar, O. (2017). Effect of the kaolinite content on porosity, permeability and capillary pressure derived parameters, Nubia sandstone, Wadi Kareem, Eastern Desert, Egypt. *Journal of African Earth Sciences, 125,* 103–117.

Khalifa, M., Soliman, H., & Wanas, H. A. (2006). The Cambrian Araba formation in northeastern Egypt: Facies and depositional environments. *Journal of Asian Earth Sciences, 27,* 873–884.

Khan, F., Enzmann, F., Kersten, M., Wiegmann, A., & Steiner, K. (2012). 3D Simulation of the permeability tensor in a soil aggregate on basis of nanotomographic imaging and LBE Solver. *J. Soil Sediment, 12*(1), 86–96.

Klitzsch, E. (1986). Plate tectonics and cratonal geology in Northeast Africa (Egypt/Sudan). *Geologische Rundschau, 75,* 755–775.

Kora, M. (1984). *The Paleozoic outcrops of Um-Bogma area, Sinai, Egypt.* Ph.D. Thesis, Mansoura University, Mansoura, Egypt, 235.

Levi, S., Nabelek, J., & Yeats, R. S. (2005). Paleomagnetism based limits on earthquake magnitudes in northwestern metropolitan Los Angeles, California, USA. *Geology, 33,* 401–404.

Lucia, F. J. (1995). Rock-fabric/petrophysical classification of carbonate pore space for reservoir characterization. *AAPG Bulletin, 79*(9), 1275–1300.

Mendelson, K. S., & Cohen, M. H. (1982). The effect of grain anisotropy on the electrical properties of sedimentary rocks. *Geophysics, 47*(2), 257–263.

Meyer, R., & Krause, F. F. (2006). Permeability anisotropy and heterogeneity of a sandstone reservoir analogue: An estuarine to shoreface depositional system in the Virgelle Member, Milk River Formation, Writing-on-Stone Provincial Park, Southern Alberta. *Bulletin of Canadian Petroleum Geology, 54*(4), 301–318.

Nabawy, B. S. (2014). Estimating porosity and permeability using digital Image analysis (DIA) technique for highly porous sandstones. *Arabian Journal of Geosciences, 7*(3), 889–898.

Nabawy, B. S. (2018). Impacts of fossil anisotropy on the electric and permeability anisotropy of highly fossiliferous limestone: A case study. *Marine Geophysical Research, 39*(4), 537–550.

Nabawy, B. S., & Al-Azazi, N. A. S. A. (2015). Reservoir zonation and discrimination using the routine core analyses data: The Upper Jurassic Sab'atayn sandstones as a case study, Sab'atayn basin, Yemen. *Arabian Journal of Geosciences, 8*(8), 5511–5530.

Nabawy, B. S., & Barakat, M Kh. (2017). Formation evaluation using conventional and special core analyses: Belayim Formation as a case study, Gulf of Suez, Egypt. *Arabian Journal of Geosciences, 10*(25), 1–23.

Nabawy, B. S., & David, Ch. (2016). X-Ray CT scanning imaging for the Nubia sandstones: A macro scale tool for characterizing fluid transport. *Geosciences Journal, 20*(5), 691–704.

Nabawy, B. S., & El Sharawy, M. S. (2015). Hydrocarbon potential, structural setting and depositional environments of Hammam Faraun Member of the Belayim Formation, Southern Gulf of Suez, Egypt. *Journal of African Earth Sciences, 112*(93), 110.

Nabawy, B. S., Elgendy, N. T. H., & Gazia, M. T. (2019). Mineralogic and diagenetic controls on reservoir quality of Paleozoic Sandstones, Gebel El-Zeit, North Eastern Desert, Egypt. *Natural Resources Research*. https://doi.org/10.1007/s11053-019-09487-4.

Nabawy, B. S., & ElHariri, T. Y. M. (2008). Electric fabric of cretaceous clastic rocks in Abu Gharadig basin, Western Desert, Egypt. *Journal of African Earth Sciences, 52*(1–2), 55–61.

Nabawy, B. S., & Géraud, Y. (2016). Impacts of pore- and petro-fabrics, mineral composition and diagenetic history on the bulk thermal conductivity of sandstones. *Journal of African Earth Sciences, 115*, 48–62.

Nabawy, B. S., Rashed, M. A., Mansour, A. S., & Afify, W. S. M. (2018). Petrophysical and microfacies analysis as a tool for reservoir rock typing and modeling: Rudeis Formation, offshore October Oil Field, Sinai. *Marine and Petroleum Geology, 97*, 260–276.

Nabawy, B. S., Sediek, K. N., & Nafee, S. A. (2015). Pore fabric assignment using electrical conductivity of some Albian-Cenomanian sequences in north Eastern Desert, Egypt. *Arabian Journal of Geosciences, 8*(8), 5601–5615.

Nabway, B. S., & Kassab, M. A. (2014). Porosity-reducing and porosity-enhancing diagenetic factors for some carbonate microfacies: A guide for petrophysical facies discrimination. *Arabian J. Geosciences, 7*(11), 4523–4539.

Perry, S. (1977). The geology of the Gebel Zeit region, Gulf of Suez, Egypt. M.Sc. Thesis, Univ. of Virginia, 85.

Perry, S., & Schamel, S. (1982). The structural evolution of Gebel El-Zeit, an arched horst, Gulf of Suez, Egypt. *Bulletin of South Carolina Academy of Science, 44*, 79.

Pittman, E. D. (1992). Relationship of porosity and permeability to various parameters derived from mercury injection capillary pressure curves for sandstone. *AAPG Bulletin, 76*, 191–198.

Rochette, P. (1987). Magnetic susceptibility of the rock matrix related to magnetic fabric studies. *Journal of Structural Geology, 9*, 1015–1020.

Said, R. (1971). Explanatory note to accompany the geological map of Egypt. *Geological Survey of Egypt, 56*, 123.

Sakran, Sh, Nabih, M., Henaish, A., & Ziko, A. (2016). Structural regime and its impact on the mechanism and migration pathways of hydrocarbon seepage in the southern Gulf of Suez rift: An approach for finding new unexplored fault blocks. *Marine and Petroleum Geology, 71*, 55–75.

Salem, A. M. K., Abdel-Wahab, A., & McBride, E. F. (1998). Diagenesis of shallow buried cratonic sandstones, southwest Sinai, Egypt. *Sedimentary Geology, 119*, 311–335.

Schlumberger. (1984). *Well Evaluation Conference*, pp. 1–64.

Schlumberger. (1995). *Well Evaluation Conference*, pp. 56–71.

Schmitt, M., Halisch, M., Müller, C., & Fernandes, C. P. (2016). Classification and quantification of pore shapes in sandstone reservoir rocks with 3-D X-ray micro-computed tomography. *Solid Earth, 7*(1), 285–300.

Schowalter, T. T. (1979). Mechanics of secondary hydrocarbon migration and entrapment. *AAPG Bulletin, 63*(5), 723–760.

Schütz, K. I. (1994). Structure and stratigraphy of the Gulf of Suez, Egypt. London, S.M. (ed.), Interior Rift Basins. *AAPG Memoir, 59*, 57–96.

Serra, O. (1988). *Fundamentals of well-log interpretation*. Amsterdam: Elsevier.

Soto-Cabán, S., & Law, L. (2013). Using resistivity measurements to determine anisotropy in soil and weathered rock. *ETASR-Engineering, Technology & Applied Science Research, 3*(4), 483–487.

Takemura, T., Golshani, A., Oda, M., & Suzuki, K. (2003). Preferred orientations of open microcracks in granite and their relation with anisotropic elasticity. *International Journal of Rock Mechanics and Mining Sciences, 40*, 443–454.

Torabi, A., & Fossen, H. (2009). Spatial variation of microstructure and petrophysical properties along deformation bands in reservoir sandstones. *AAPG Bulletin, 93*, 919–938.

Veloso, F. M. L., Navarrete, R., Soria, A. R., & Meléndez, N. (2016). Sedimentary heterogeneity and petrophysical characterization of Barremian tsunami and barrier island/inlet deposits: The Aliaga outcrop as a reservoir analogue (Galve Sub-Basin, eastern Spain). *Marine and Petroleum Geology, 73*, 188–211.

Wanas, H. A. (2011). The Lower Paleozoic rock units in Egypt: An overview. *Geoscience Frontiers, 2*(4), 491–507.

Winland, H. D. (1972). Oil accumulation in response to pore size changes, Weyburn field, Saskatchewan. *Amaco Production Research Report No. F72-G-25*.

Youssef, A. (1986). Coastal to shallow marine facies in Zeit Bay area, Gulf of Suez, Egypt. In: 8th EGPC Expl. Conf. Cairo, pp. 344–358.

Zein El-Din, M. Y., & Taher, M. (1973). *Contribution of dipmeter analysis to the history of West Gebel El-Zeit Basin, Gulf of Suez*. Ann. Meet. Geol. Soc. Egypt, Cairo.